Energy Materials and Devices

Open Access
Research Article

Graphical Abstract

Vanadium nitride/carbon fiber engineered with oxygen defects and vertically aligned nanosheets for high-rate flexible aqueous zinc-ion batteries

Zhouyang Qin[1], Gaoxu Han[2], Yilin Yang[1], Wenjie Zhang[3] ✉, Ruitao Lv[1], Wanci Shen[1], and Zheng-Hong Huang[1] ✉

[1] *Key Laboratory of Advanced Materials (MOE), State Key Laboratory of New Ceramics and Fine Processing, School of Materials Science and Engineering, Tsinghua University, Beijing 100084, China*
[2] *School of Chemical and Environmental Engineering, China University of Mining and Technology (Beijing), Beijing 100083, China*
[3] *Institute for Energy Research, Jiangsu University, Zhenjiang 212013, China*

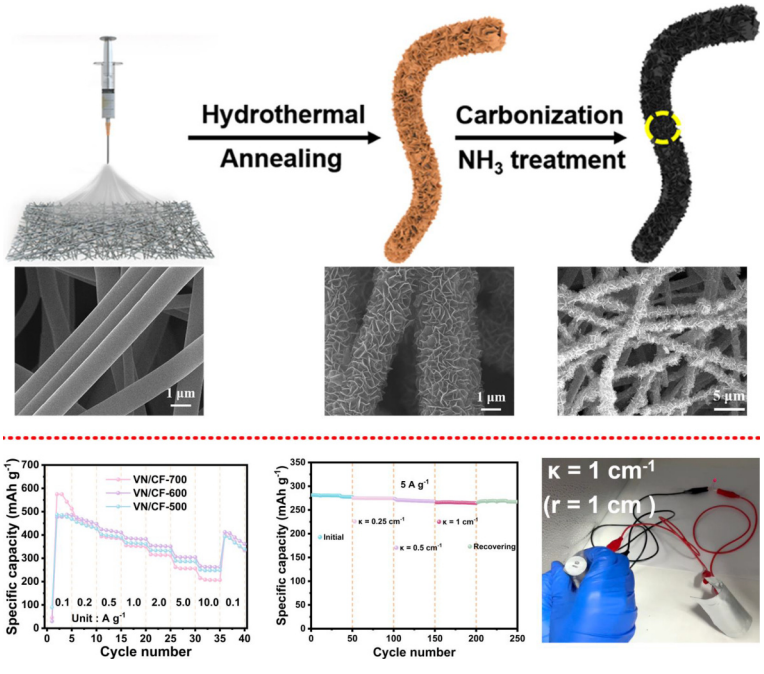

This study presents a free-standing vanadium nitride/carbon fiber cathode with oxygen defects and vertically aligned porous nanosheets, which synergistically enhance the kinetics of bulk and surface diffusion, enabling excellent rate capability. The assembled flexible zinc-ion battery maintains stable performance under bending, showing great potential for wearable devices.

✉Address correspondence to **Wenjie Zhang**, zwenjie@ujs.edu.cn; **Zheng-Hong Huang**, zhhuang@tsinghua.edu.cn

Received: November 20, 2025
Revised: January 5, 2026
Accepted: January 7, 2026

9370086

Read Online

Citation: Qin Z., Han G., Yang Y., et al. Vanadium nitride/carbon fiber engineered with oxygen defects and vertically aligned nanosheets for high-rate flexible aqueous zinc-ion batteries. *Energy Mater. Devices*, 2026, 4(1), 9370086. https://doi.org/10.26599/EMD.2026.9370086

Open Access This article is licensed under a Creative Commons Attribution 4.0 International License (CC BY 4.0), which permits reusers to distribute, remix, adapt, and build upon the material in any medium or format, so long as attribution is given to the original author(s) and the source, a link to the license is provided, and any changes made are indicated. See https://creativecommons.org/licenses/by/4.0/

© The author(s) 2026. Published by Tsinghua University Press.

Energy Materials and Devices
https://doi.org/10.26599/EMD.2026.9370086
Open Access
Research Article

Vanadium nitride/carbon fiber engineered with oxygen defects and vertically aligned nanosheets for high-rate flexible aqueous zinc-ion batteries

Zhouyang Qin[1], Gaoxu Han[2], Yilin Yang[1], Wenjie Zhang[3] ✉, Ruitao Lv[1], Wanci Shen[1], and Zheng-Hong Huang[1] ✉

[1] *Key Laboratory of Advanced Materials (MOE), State Key Laboratory of New Ceramics and Fine Processing, School of Materials Science and Engineering, Tsinghua University, Beijing 100084, China*
[2] *School of Chemical and Environmental Engineering, China University of Mining and Technology (Beijing), Beijing 100083, China*
[3] *Institute for Energy Research, Jiangsu University, Zhenjiang 212013, China*

Cite this article: *Energy Mater. Devices* 2026, **4**(1): 9370086. https://doi.org/10.26599/EMD.2026.9370086

ABSTRACT

Flexible aqueous zinc-ion batteries (AZIBs) are promising candidates for wearable devices owing to their high safety and low cost. However, their progress is plagued by their sluggish ion-transport kinetics, which leads to inferior rate capability. Herein, a vanadium nitride/carbon fiber (VN/CF) cathode was structurally engineered to incorporate oxygen defects and a vertically aligned, porous, nanosheet architecture to overcome these issues. This structure was realized via the initial growth of vertically aligned V_2O_5 nanosheet templates on gas-spun carbon fibers, followed by high-temperature NH_3 treatment. The oxygen defects accelerate the kinetics of bulk diffusion within VN, while the vertically aligned VN nanosheet array possesses lower charge-transfer resistance, enhancing the kinetics of surface diffusion. These features synergistically improve the overall Zn^{2+} transport, affording high-rate performance. Consequently, the free-standing VN/CF cathode exhibits exceptional rate performance, delivering a capacity of 263.4 mAh g^{-1} even at a high current density of 10 A g^{-1}. When assembled into flexible AZIBs, the device exhibits a high-rate capability of 249.7 mAh g^{-1} at 10 A g^{-1} and stable performance even under various bending deformations, demonstrating significant potential for next-generation wearable devices.

KEYWORDS

aqueous zinc-ion batteries, oxygen defects, vertically aligned porous nanosheet, high-rate performance

1 Introduction

Flexible energy-storage devices have promising applications in wearable electronics, health monitoring, medical applications, etc.[1–7]. To meet the demands of flexible electronics, the energy-storage devices must possess high energy/power density and excellent flexibility, while being durable and safe[8–16]. Compared with lithium-ion and sodium-ion batteries that rely on flammable organic electrolytes, aqueous batteries utilize aqueous electrolytes with high ionic conductivity, ensuring high safety and stable operation under mechanical deformation[17–24]. Among them, aqueous zinc-ion batteries (AZIBs) have garnered increasing interest owing to their inherent safety, relatively low redox potential (−0.76 V vs. standard hydrogen electrode), low toxicity, and minimal environmental impact, as well as the abundance of zinc resources and high theoretical specific capacity of the zinc anode (820 mAh g^{-1})[25–30]. Cathode materials are a critical factor limiting the performance and practical application of AZIBs[31–33]. Among various candidates, transition-metal nitrides possess a metal-like, continuous energy-band structure, which results from their conduction bands, formed by the hybridization of metal d-orbitals and nitrogen 2p-orbitals, yielding a broad energy-band[34–37]. Consequently, these materials demonstrate superior electrical conductivity, which facilitates efficient charge transport[38–40]. Within the category of transition-metal nitrides, vanadium nitride (VN) is a highly promising cathode material for AZIBs owing to its high theoretical specific capacity (825 mAh g^{-1}) and outstanding electrical conductivity (10^4–10^6 S m^{-1})[41–43].

However, the dense face-centered cubic structure of VN inherently limits Zn^{2+} diffusion[44–49], leading to poor rate capability. To address these limitations, strategies such as nanoengineering, defect engineering, and the design of composite structures have been widely explored[50–53]. Nanoengineering can effectively shorten the ion-diffusion pathways and increase the number of electrochemically active sites, thereby improving charge transport. Conse-

Received: November 20, 2025 / **Revised:** January 5, 2026 / **Accepted:** January 7, 2026

✉ **Address correspondence to** Wenjie Zhang, zwenjie@ujs.edu.cn; Zheng-Hong Huang, zhhuang@tsinghua.edu.cn

quently, diverse VN nanostructures such as nanorods, nanosheets, and quantum dots have been synthesized for achieving enhanced electrochemical performance[54–57]. Recent studies have also highlighted the role of defect engineering in facilitating ion transport. Introducing defects into the VN lattice creates additional pathways for ion diffusion, which accelerates Zn^{2+} transport. Accordingly, researchers have developed oxygen-defect-rich VN[43,58–61], nitrogen-vacancy-rich VN[42], and Al-doped VN[62]. Moreover, rational structural design by hybridizing VN with conductive materials is effective for improving the electronic conductivity. Representative composite architectures have been constructed using carbon nanofibers[63,64], carbon matrices[65–69], rGO[70–73], carbon nanotubes (CNTs)[74], and MXene[75,76]. Despite these advances, fundamental challenges persist, particularly regarding the high intrinsic charge-transfer resistance of VN. Additionally, the conventional powder morphology of VN lacks mechanical flexibility, and traditional slurry-cast electrodes suffer from delamination of the active material under mechanical stress, limiting their applicability in flexible energy-storage devices.

Herein, to address these challenges, we design a free-standing VN/carbon fiber (VN/CF) with oxygen defects and a vertically aligned, porous nanosheet architecture. The structure was created by first growing vertically aligned V_2O_5 nanosheets on gas-spun carbon fibers, followed by high-temperature NH_3 treatment. The carbon fiber network provides a continuous conductive framework and mechanical flexibility. Oxygen defects engineered in VN provide additional diffusion channels and active sites for Zn^{2+}, enhancing the kinetics of bulk diffusion. The charge-transfer resistance at the surface of the vertically aligned VN nanosheet arrays is relatively low and the structure facilitates rapid ion transport, thereby enhancing the kinetics of surface diffusion. These synergistic structural features promote Zn^{2+} transport and enable outstanding rate capability. Consequently, the VN/CF cathode demonstrates superior rate performance, achieving a remarkable specific capacity of 263.4 mAh g^{-1} at 10 A g^{-1}. Moreover, the pouch cell assembled with the VN/CF cathode exhibits a high-rate capability of 249.7 mAh g^{-1} at 10 A g^{-1} and maintains stable performance under bending, demonstrating its potential for flexible energy-storage applications.

2 Materials and methods

2.1 Chemicals

The chemicals used in the experiments and their sources are as follows: polyacrylonitrile (PAN; AR, Aladdin), *N,N*-dimethylformamide (DMF; AR, Adamas), vanadium triisopropoxy oxide (VOT; 97%, Shanghai Macklin Biochemical Co., Ltd.), hexadecyl trimethyl ammonium bromide (CTAB; 99%, Sinopharm Chemical Reagent Co., Ltd.), and isopropyl alcohol (C_3H_8O; AR, Sinopharm Chemical Reagent Co., Ltd.).

2.2 Fabrication of PAN-CF

A precursor solution was prepared by dissolving 0.75 g PAN in 5 mL DMF, followed by heating for 6 h at 45°C in a water-bath with stirring to achieve a transparent viscous solution, which was subsequently degassed via ultrasonication. The carbon fiber membrane was fabricated through gas-spinning using 3 mL of this solution loaded into a syringe equipped with a 30 G needle. A permeable, white, non-woven fabric was positioned 15 cm away as the collector. The syringe propulsion rate was 1.5 mL min^{-1} and the flow rate of the power gas was 15–30 L min^{-1}. Post-spinning, the solvent in the membrane was removed by drying for 6 h at 80°C, followed by preoxidation by ramping the temperature to 260°C at 2°C min^{-1}, with a 2 h isothermal hold. Subsequent carbonization at 700°C under 200 sccm Ar flow for 2 h yielded the PAN-CF flexible substrate for hydrothermal growth.

2.3 Preparation of VN/CF-T

A precursor solution was prepared by dissolving 400 mg VOT and 600 mg CTAB in 70 mL isopropanol and stirring for 30 min. The mixture was then transferred to a 100 mL polytetrafluoroethylene (PTFE) liner containing a 3 cm × 4 cm PAN-CF membrane for hydrothermal treatment in the sealed vessel by ramping the temperature to 180°C at 3°C min^{-1}, followed by isothermal reaction for 12 h and cooling in the furnace. The resulting membrane was washed with ethanol multiple times then vacuum dried at 60°C for 12 h to yield Product 1. Annealing Product 1 at 300°C under ambient atmosphere for 1 h produced Product 2, characterized by a uniform, yellow surface coating. Subsequent activation by nitridation in a tube-furnace under NH_3:Ar = 3:1 atmosphere by heating to 600°C at 5°C min^{-1} with a 2 h dwell time yielded VN/CF-600. For comparison, samples VN/CF-500 and VN/CF-700 were identically processed at 500°C and 700°C, respectively.

2.4 Material characterization

The morphology of the samples was examined using scanning electron microscopy (SEM; HITACH S4800) and transmission electron microscopy (TEM; Tecnai G20, 200 kV). The phase and phase-change of the cathodes were examined using an X-ray diffractometer (XRD; Bruker D8-Advance) with Cu Kα radiation (λ = 1.5406 Å). Raman spectra were acquired using a Raman microscope (LabRAM HR, 532 nm). The chemical composition and valence states of the elements were determined using X-ray spectroscopy (XPS; PHI5300). The absorption and desorption curves and specific surface areas of the prepared samples were determined from the nitrogen adsorption data acquired with a Quantachrome Instruments apparatus (Boynton Beach, USA) using the Brunauer–Emmett–Teller (BET) method. The pore-size distribution was calculated using the density functional theory method.

2.5 Electrochemical measurements

The electrochemical performance of the prepared cathodes was evaluated in CR2032-type coin and pouch cells. All cells were assembled under ambient atmosphere using a 2 mol/L aqueous $Zn(CF_3SO_3)_2$ solution as the electrolyte, one layer of glass fiber membrane (Whatman GF/D) as the separator, and Zn foil with a thickness of 50 μm as the anode. Cyclic voltammetry (CV) and electrochemical

impedance spectroscopy (EIS) measurements were conducted using a Biologic VSP-300 device. The voltage windows of the prepared cathodes spanned 0.01–1.5 V (vs. Zn/Zn^{2+}). EIS data were recorded over the frequency range of 100 mHz to 100 kHz. Galvanostatic intermittent titration (GITT) was performed to determine the diffusion coefficient of Zn^{2+} using a battery testing system (LANHE, CT3002A). For fabrication of the pouch cells, VGS-811 with a diameter of 4 cm and Zn foil were packaged with Al-plastic film. The galvanostatic charge–discharge (GCD) tests were conducted on a LANHE CT3002A instrument over the voltage window of 0.01–1.5 V. All electrochemical measurements were performed in full-cell configurations with Zn metal as the anode and the active material as the cathode. The values shown in the CV and GCD curves correspond to the measured potential difference between the two electrodes.

3 Results and discussion

Figure 1a schematically illustrates the fabrication of the free-standing VN/CF-T. The resulting VN/CF-600 features abundant oxygen defects, vertically aligned porous nanosheets, and deliberately tuned low crystallinity. To realize this unique structure, we developed a controllable synthesis strategy in which vertically aligned V_2O_5 nanosheet templates are grown on gas-spun carbon fibers, followed by high-temperature NH_3 treatment. This approach achieves multiple objectives: (1) V_2O_5 serves as both the vanadium source and the source of the oxygen dopant in VN; (2) the vertically aligned V_2O_5 nanosheets serve as a template that induces the formation of orientation-consistent VN nanosheets; (3) gas release and lattice reconstruction during the high-temperature reduction create pores within the VN nanosheets; and (4) temperature-controlled reduction moderates low crystallinity. Initially, a carbon fiber membrane substrate (PAN-CF) was fabricated via gas-spinning coupled with high-temperature carbonization. SEM imaging reveals fibers with diameters ranging from several hundred nanometers to 2 μm (Figs. S1a–S1c in Supplementary Material). Subsequently, $V_5O_{12}{\cdot}6H_2O$ nanosheets were vertically grown on PAN-CF through hydrothermal synthesis (Fig. S1d–S1f, and S4 in Supplementary Material). TEM analysis indicated thicknesses of approximately several tens of nanometers (Fig. 1e). The sample was annealed at 300°C

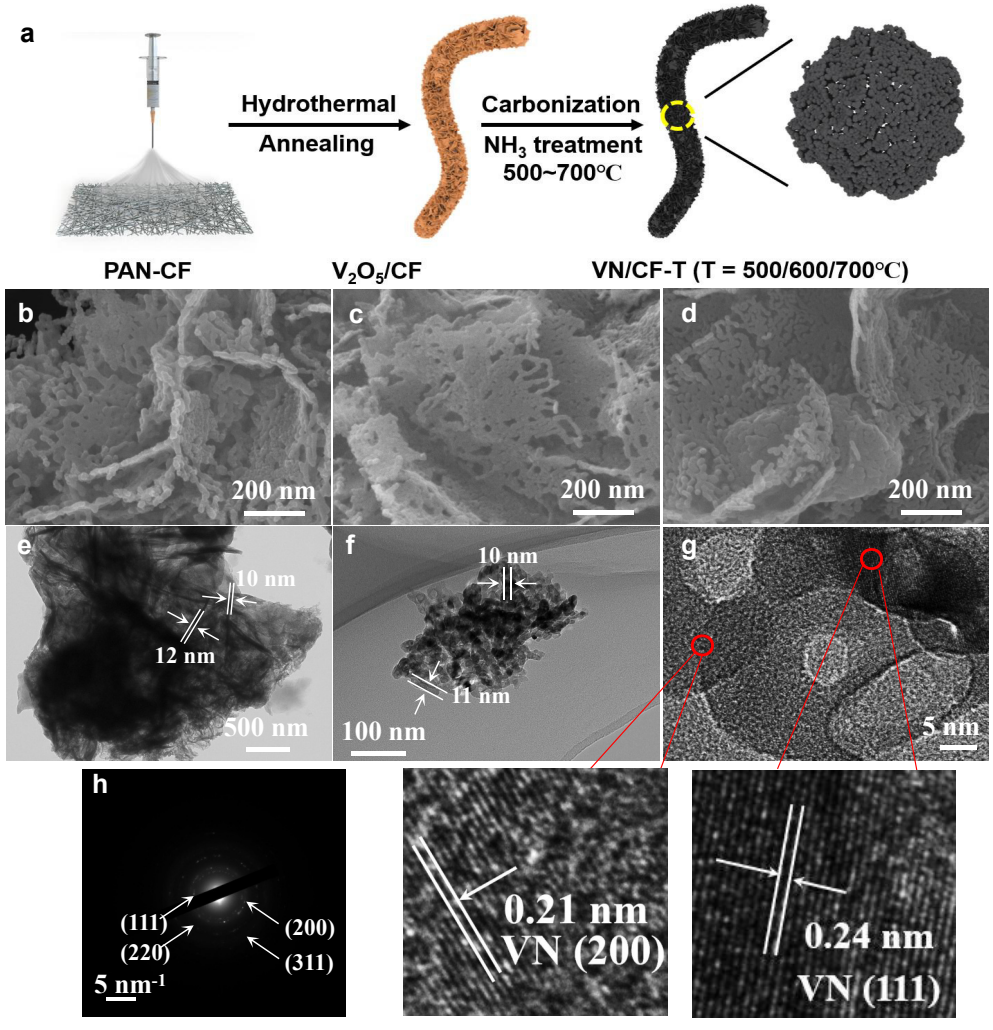

Figure 1 Synthesis and characterization of prepared cathodes. (a) Schematic of VN/CF-T synthesis. SEM images of VN/CF-500 (b), VN/CF-600 (c), and VN/CF-700 (d). (e) TEM images of the product after hydrothermal synthesis. TEM (f), high-resolution TEM (HRTEM) (g), and selected area electron diffraction (SAED) (h) images of VN/CF-600.

under ambient atmosphere for 1 h to yield V_2O_5/CF (Fig. S4 in Supplementary Material). As shown in Figs. S1g–S1i in Supplementary Material, V_2O_5 retained the nanosheet morphology and dimensions, whereas nanopores emerged within the V_2O_5 nanosheet. This porosity is attributed to volumetric shrinkage caused by the loss of water-of-crystallization during annealing. Subsequently, V_2O_5/CF was treated with NH_3 at 600°C to generate a vertically aligned, porous VN nanosheet array on CF (VN/CF-600), as shown in Figs. 1a, 2a, and Fig. S2 in Supplementary Material. The TEM image of VN/CF-600 reveals stacked VN nanoparticles with diameters of approximately 10 nm and numerous interparticle pores (Fig. 1f). HRTEM shows lattice fringes with interplanar spacings of 0.24 and 0.21 nm, corresponding to the (111) and (200) planes of VN, respectively (Fig. 1g). The SAED pattern shows four diffraction rings matching the (111), (200), (220), and (311) planes of VN (Fig. 1h). Energy-dispersive spectroscopy analysis of VN/CF-600 confirms the presence of V and N (Fig. S3 in Supplementary Material).

The control VN/CF-500 and VN/CF-700 samples were prepared by treating V_2O_5/CF with NH_3 at 500°C and 700°C. VN/CF-500 is structurally similar to VN/CF-600, with vertically aligned, porous VN nanosheet arrays on the carbon fiber substrate (Fig. 1b, Figs. S2a and S2b in Supplementary Material). In the case of VN/CF-700, partial destruction of the vertical nanosheets and their agglomeration into larger particles on the carbon fibers are observed (Fig. 1d, Figs. S2e and S2f in Supplementary Material). This is caused by volumetric contraction during transition of the crystal structure at higher temperatures[77].

XRD analysis of the full-width-at-half-maximum (FWHM) of the (002) peak demonstrates values of 0.96°, 0.68°, and 0.26° at 500°C, 600°C, and 700°C, respectively (Fig. 2a). Analysis using the Scherrer equation indicates an increase in the grain size and crystallinity of VN at higher temperatures. The specific surface areas of VN/CF-500, VN/CF-600, and VN/CF-700 are 253, 294, and 41 $m^2\ g^{-1}$, respectively (Fig. 2b and Fig. S5 in Supplementary Material). Increasing the temperature from 500°C to 600°C enhances both the specific surface area and pore volume. This improvement correlates with the reduced particle size of VN observed by SEM, which provides more surfaces and multiscale porosity. At 700°C, the surface area decreased sharply owing to loss of the micropores and a slight increase in the number of mesopores, caused by grain coarsening of VN, sheet-like aggregation, and structural degradation of the vertically aligned nanosheets.

Raman analysis (Fig. 2c) shows characteristic VN peaks at 139, 277, 403, and 989 cm^{-1}[78]. The intensity of the peaks was lowest for VN/CF-600, indicating substantial lattice defects[42]. Complementary EPR characterization of V_2O_5/CF and VN/CF-T (Fig. 2d) revealed centrosymmetric intensity curves at $g = 2.003$, confirming the presence of oxygen defects in all materials[55,79]. The XRD results confirm that VN/CF-T contains only the VN phase, with no detectable V_2O_5 or other oxides (Fig. 2a). This indicates that oxygen mainly exists in the form of a dopant within the VN lattice rather than as oxygen vacancies. The symmetrical EPR signal at $g = 2.003$ for VN/CF-T is attributed to lattice distortion and nitrogen vacancies induced by oxygen doping[42,80]. For the V_2O_5/CF sample, the EPR signal arises from oxygen vacancies present in V_2O_5. The oxygen defects are generated in VN through the removal of crystallization water and the V_2O_5-to-VN phase transformation during high-temperature annealing under NH_3 atmosphere. Quantitative analysis indicates that VN/CF-600 displays marginally higher EPR peak intensity than VN/CF-500, corresponding to a slightly higher concentration of oxygen defects; VN/CF-700 had the lowest defect content. This trend primarily stems from the accelerated diffusion of reactive nitrogen derived from NH_3 decomposition and its sufficient reaction with vanadium at elevated temperatures, which suppresses the formation of oxygen defects.

XPS analysis indicates differences in the elemental composition and chemical environment of VN/CF-T versus V_2O_5/CF across temperatures. Figure S6a in Supple-

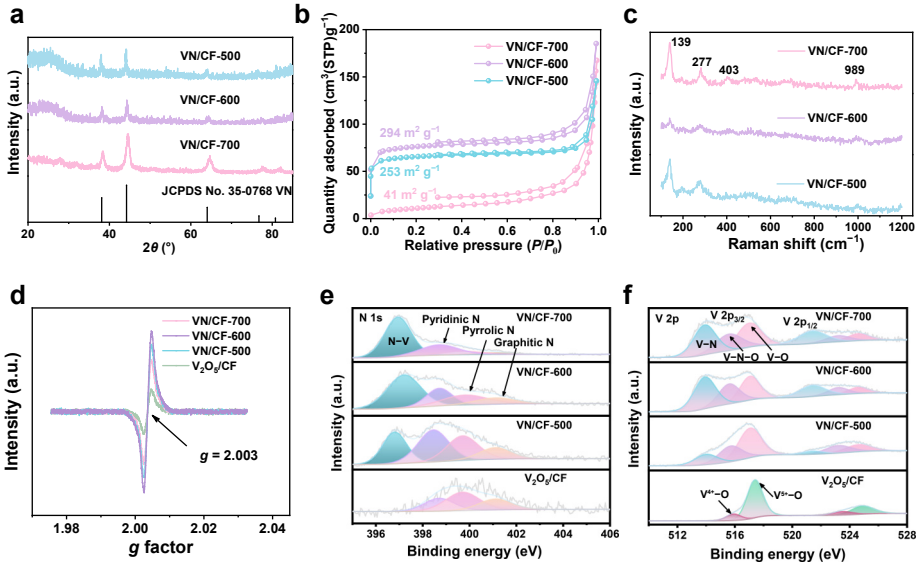

Figure 2 XRD patterns (a), N_2 adsorption/desorption curve (b), Raman spectra (c), electron paramagnetic resonance (EPR) spectra (d), N 1s (e) and V 2p (f) high-resolution XPS profiles of V_2O_5/CF and VN/CF-T.

mentary Material confirms the presence of C, N, O, and V across all samples, where C is derived from the PAN-CF substrate and the trace N in V_2O_5/CF similarly originates from PAN. Oxygen in VN/CF-T is derived from both surface oxidation of VN and residual O from incomplete NH_3 reduction of V_2O_5[74]. The high-resolution spectra (Figs. S6b and S6c in Supplementary Material) demonstrate a decrease in the O content with increasing reduction temperature. The N 1s XPS profile (Fig. 2e) reveals intensified N-V bonding post NH_3 treatment. The V 2p XPS profile is shown in Fig. 2f. From the V 2p spectrum, V^{4+}-O (515.9 eV, 523.5 eV) and V^{5+}-O (517.4 eV, 524.9 eV) are identified in V_2O_5/CF[40], where the V^{4+}-O signals indicate incomplete oxidation during annealing, generating oxygen vacancies. The V 2p XPS profiles of the VN/CF-T samples were deconvoluted into three contributions: V-N (513.9 eV, 521.4 eV), V-N-O (515.6 eV, 523.2 eV), and V-O (517.1 eV, 524.6 eV)[64].

Coin-type ZIBs were assembled using 2 mol/L $Zn(CF_3SO_3)_2$ electrolyte and the prepared cathodes with mass loadings of 1.2-1.5 mg cm^{-2}. The batteries were tested within the potential window of 0.01-1.5 V (vs. Zn^{2+}/Zn). Figure 3a reveals minimal peak currents during the first scan, correlating with a lower specific discharge capacity in the initial GCD cycle (Fig. 3b) and diminished charge capacity at 1.25 V. These observations collectively indicate sluggish electrochemical kinetics, insufficient active sites, and inferior zinc-ion storage. A distinct redox peak appears at 1.25-1.5 V in the first forward scan, which corresponds to the extended charging plateau above 1.25 V. The long tails observed at 1.5 V in the CV curves may be associated with the occurrence of side-reactions, activation of internal ion-diffusion channels, and an increase in the number of electrochemical reaction sites[81,82]. After activation, the subsequent CV curves of VN/CF-600 display two prominent redox peak pairs at 1.04/0.91 V and 0.70/0.52 V. These align with the charge-discharge plateaus in the subsequent cycles, confirming a two-step reaction pathway[83]. Analysis of the rate performance reveals that PAN-CF exhibits limited specific capacity only below 0.2 A g^{-1}, while PAN-CF-NH_3 demonstrates a capacity retention up to 2 A g^{-1} (Fig. S8 in Supplementary Material). In both capacitive cathodes, the capacity is derived primarily from the surface adsorption of Zn^{2+}. V_2O_5/CF delivers 219 mAh g^{-1} at 0.1 A g^{-1} but rapidly degrades to near-zero capacity at 5 A g^{-1}. In contrast, VN/CF-T demonstrates better performance. The specific capacities of VN/CF-500, VN/CF-600, and VN/CF-700 are 468.4, 485.4, and 512.7 mAh g^{-1} after 5 cycles at 0.1 A g^{-1}, respectively (Fig. 3c). With increasing current density, the change in the capacity indicates minimal decay for VN/CF-600 versus maximal degradation for VN/CF-700, yielding 263.4 mAh g^{-1} versus 206.7 mAh g^{-1}, respectively, at 10 A g^{-1}. VN/CF-600 exhibits exceptional cyclic stability, with a high specific capacity of 284.3 mAh g^{-1} and capacity retention of 92.3% at 5 A g^{-1} after 8000 cycles (**Fig. 3f**). It also maintains a Coulombic efficiency (CE) above 99.18% during cycling at 0.5, 1 and 5 A g^{-1}, as well as throughout

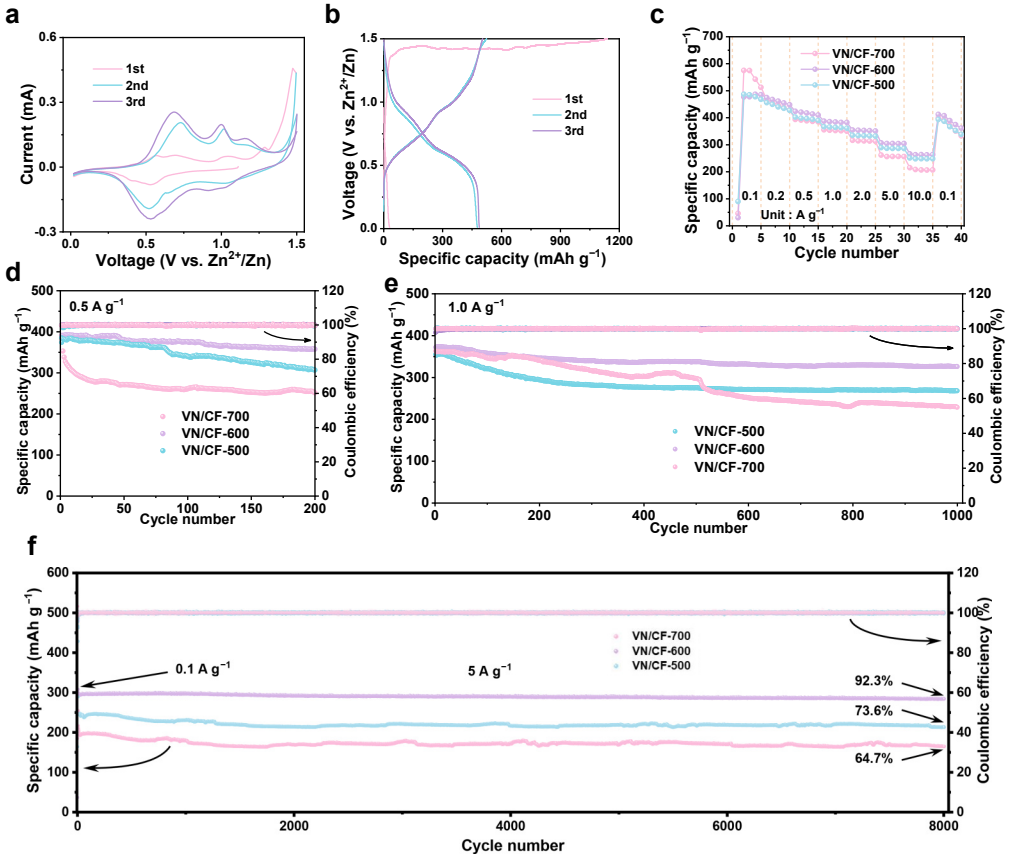

Figure 3 Electrochemical performance of prepared cathodes. (a) Initial three CV curves of VN/CF-600 at 0.2 mV s^{-1}. (b) GCD curves of VN/CF-600 at 0.1 A g^{-1}. Rate capability (c), cycle performance at 0.5 A g^{-1} (d), 1.0 A g^{-1} (e), and 5 A g^{-1} (f) of VN/CF-T.

8000 long-term cycles, indicating highly reversible electrochemical reactions. Benchmarking against prior studies (Fig. S9 in Supplementary Material) confirms the superior rate capability of VN/CF-600, particularly in delivering high capacity at high current densities and maintaining cycling durability at 5 A g^{-1}. The outstanding performance can be attributed to the design of oxygen defects and the vertically aligned, porous nanosheet architecture of VN/CF-600. Among the samples, VN/CF-600 has the highest concentration of oxygen defects. These defects induce lattice expansion in the VN structure, as evidenced by the shift in the XRD peaks toward lower angles (Fig. 2a), which enlarges the Zn^{2+} transport channels. Furthermore, oxygen substitution for nitrogen creates vacancy defects, providing additional Zn^{2+}-transport pathways. These effects accelerate the kinetics of bulk diffusion within VN, while the vertically aligned VN nanosheet array possesses lower charge-transfer resistance, which enhances the kinetics of surface diffusion. This behavior arises from two main factors. First, the vertically aligned nanosheet array exposes a larger and more accessible electroactive surface[84–86]. Second, the low tortuosity of this configuration enhances the effective ion-diffusion coefficient (D_{eff})[87] according to the equation $D_{eff} = D(\varepsilon/\tau)$, where ε is the porosity, τ is the tortuosity, and D is the ionic conductivity, D_{eff} is inversely proportional to τ[88,89]. Therefore, compared to conventional disordered electrodes, the vertically aligned arrays enable more efficient ion diffusion. Collectively, these features synergistically improve the overall efficiency of Zn^{2+} transport, thus endowing VN/CF-600 with excellent high-rate performance. Moreover, compared to the bulk material, the thin nanosheet and porous structure of VN facilitates efficient electrolyte infiltration, enhancing the utilization of VN and maximizing access to its intrinsic capacity.

In addition, VN/CF-700 affords a larger capacity at 0.1 A g^{-1} but lower capacities at 0.5–10 A g^{-1}, compared with VN/CF-500 and VN/CF-600 (Fig. 3c). This phenomenon is likely related to the crystallinity of the samples. At a low current density (0.1 A g^{-1}), the increasing capacity trend aligns well with the enhanced crystallinity. As shown by the XRD analysis (Fig. 2a), the VN/CF-700 sample exhibits stronger VN diffraction peaks and a narrower FWHM (0.26°) compared to VN/CF-600 (0.68°) and VN/CF-500 (0.96°), indicating that VN/CF-700 synthesized at higher temperatures has higher crystallinity. This suggests that higher crystallinity enhances the capacity at low current densities. However, this trend is reversed at high current densities, where VN/CF-700 delivers a lower capacity than VN/CF-500 and VN/CF-600. At high current densities, the capacity is limited by the ion-diffusion kinetics. Highly crystalline VN has a dense, ordered face-centered cubic lattice with low defect density, which in turn inhibits rapid diffusion of Zn^{2+}within VN. This leads to insufficient bulk reactions and poor rate performance. Additionally, repeated Zn^{2+} insertion/extraction induces greater lattice strain in highly crystalline VN, increasing the risk of particle pulverization and capacity decay. Conversely, moderately reduced crystallinity facilitates Zn^{2+} diffusion and alleviates the cyclic lattice strain. Consequently, VN/CF-600 and VN/CF-500 with lower crystallinity and higher defect densities demonstrate better rate capability and cycling stability compared to VN/CF-700.

To investigate the reversibility of Zn^{2+} insertion/extraction and the formation of intermediate phases, *ex situ* XRD was performed at 1.5 V (fully charged), 0.01 V (fully discharged), and other voltages (intermediate states). As shown in Figs. 4a and 4b, only diffraction peaks of VN and the stainless-steel sheet are observed at 1.5 V. During discharge, the (111) peak at 37.6° in the profile of VN shifts to lower angles, indicating lattice expansion owing to Zn^{2+} insertion. Upon charging, the peak shifts back to nearly its original position, corresponding to Zn^{2+} extraction[75]. Two new diffraction peaks appear at 12.3° and 30.5° during discharge, assigned to the (001) and (012)

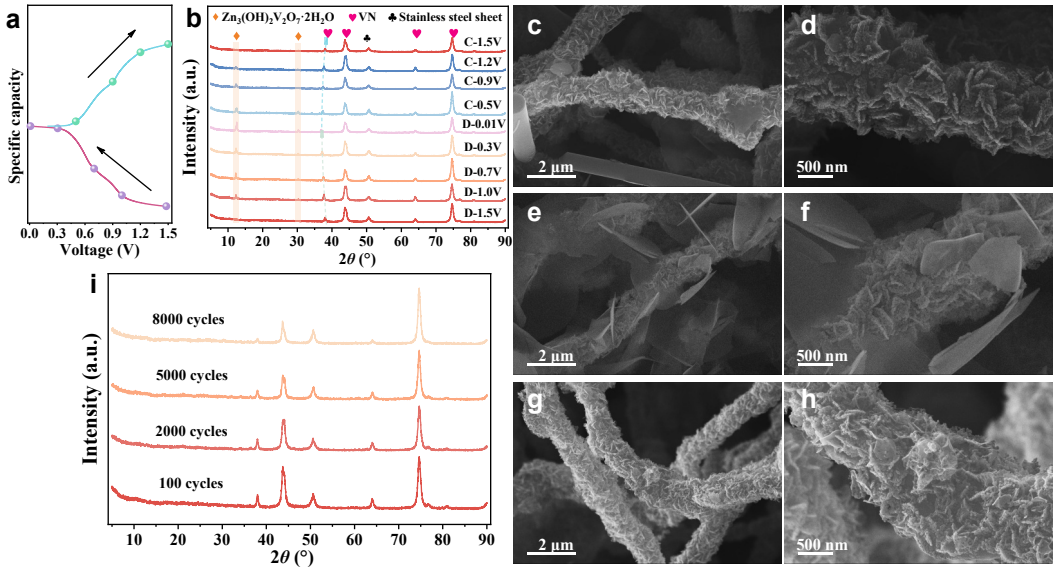

Figure 4 *Ex situ* characterization of VN/CF-600 electrode after 100 cycles. (a) Characteristic voltage profile of GCD. (b) *Ex situ* XRD patterns. SEM images at different voltages: 1.5 V (before discharge) (c–d), 0.01 V (fully discharged) (e–f), and 1.5 V (fully charged) (g–h). (i) XRD patterns after different cycles.

planes of the $Zn_3(OH)_2V_2O_7{\cdot}2H_2O$ (ZVO) byproduct[90]. The intensity of these peaks increases during discharge and decreases upon charging, and the peaks disappear at 1.5 V. These *ex situ* XRD results demonstrate that both Zn^{2+} insertion/extraction and ZVO formation/decomposition proceed in a highly reversible manner. *Ex situ* SEM was further employed to track the morphological evolution. As shown in Figs. 4c and 4d, the VN/CF-600 electrode maintains its original vertically aligned VN nanosheet morphology on the carbon fibers after 100 cycles in the fully charged state. When fully discharged to 0.01 V, micron-sized ZVO sheets are observed on the surface of VN (Figs. 4e and 4f). Upon recharging to 1.5 V, these ZVO sheets disappear and the morphology of the electrode largely recovers to its pre-discharge state (Figs. 4g and 4h). The XRD patterns acquired after 100, 2000, 5000, and 8000 cycles indicate VN as the dominant phase, without signs of irreversible vanadium dissolution or phase degradation (Fig. 4i). These *ex situ* characterizations demonstrate that VN/CF-600 exhibits excellent structural stability and highly reversible phase evolution during Zn^{2+} insertion/extraction.

The combination of remarkable structural integrity and highly reversible electrochemical processes supports the excellent cycling stability of VN/CF-600. This sustained stability plausibly originates from the porous nanosheet architecture, low crystallinity, and high concentration of oxygen defects in VN/CF-600. The pores within the VN nanosheets accommodate volume expansion and release stress induced by Zn^{2+} insertion/extraction, while low-crystallinity VN with abundant defects mitigates cyclic lattice strain during cycling. Additionally, the abundant oxygen defects enhance the kinetics of Zn^{2+} transport. Together, these features enable highly reversible reactions and prevent structural degradation, thereby supporting excellent long-term cycling stability.

The reaction kinetics of VN/CF-T were further investigated. In the VN/CF-T series, VN/CF-600 possesses the highest concentration of oxygen defects, followed by VN/CF-500 and VN/CF-700. As the scan rate increases from 0.2 to 10 mV s^{-1}, VN/CF-600 retains two pairs of well-defined redox peaks at 1.04/0.91 and 0.70/0.52 V (Fig. 5a). In contrast, VN/CF-700 exhibits severe peak distortion above 2 mV s^{-1}, where the 0.70/0.52 V peaks vanish and the polarization increases significantly (Fig. S10b in Supplementary Material). Compared with VN/CF-500 (Fig. S10a in Supplementary Material), which shares a similar vertically aligned nanosheet array morphology, the redox peaks of VN/CF-600 are more stable and there is less distortion at high scan rates. These results indicate that oxygen defects promote Zn^{2+} diffusion within bulk VN, supporting the redox reactions and diffusion-controlled capacity. The diffusion and capacitive contribution ratios were analyzed from the relationship $i = k_1\nu + k_2\nu^{1/2}$. The results reveal that VN/CF-600 exhibits a high capacitive contribution of over 75%, indicating that the capacitive contribution accounts for a higher proportion of the total capacity. This is attributed to its vertically aligned, porous nanosheet array morphology, which provides a larger and more accessible electroactive surface, and the low-tortuosity ion-transport pathways, which enhance the effective ion-diffusion coefficient. Both factors significantly improve the kinetics of surface diffusion, resulting in a larger capacitive contribution. Owing to the enhanced ion-diffusion kinetics, VN/CF-600 demonstrates a higher capacitive contribution ratio than VN/CF-500 and VN/CF-700 (Figs. S10c and S10d in Supplementary Material). GITT analysis also reveals a higher Zn^{2+} diffusion coefficient for VN/CF-600 (Figs. 5d and 5f). This is attributed to VN/CF-600 possessing the highest oxygen defect concentration and a more favorable vertically aligned VN nanosheet array.

In a device-level evaluation, VN/CF-600 was used as a free-standing cathode in flexible zinc-ion batteries. The extended plateau in the initial charging curve (Fig. 6a) signifies an activation process. Subsequent GCD cycles exhibit distinct plateaus at 1.02/0.89 and 0.71/0.57 V, confirming persistent two-step electrochemical reactions

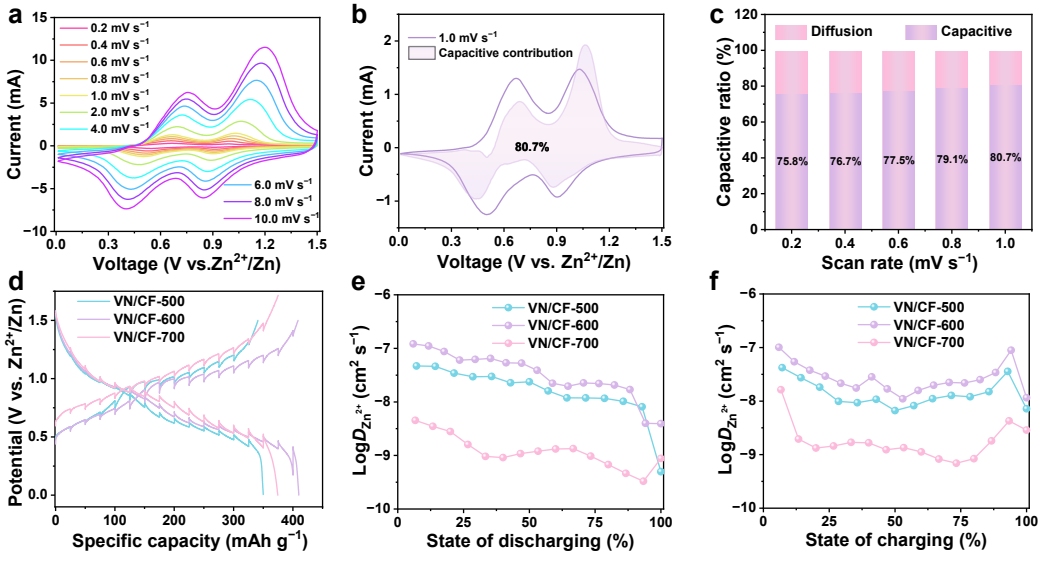

Figure 5 Reaction kinetics of VN/CF-T. (a) CV curves at different scan rates from 0.2 to 10 mV s^{-1}. (b) Capacitive contributions at 0.2 mV s^{-1}. (c) Capacity contribution ratios of VN/CF-600 at various scan rates. (d) Discharge/charge GITT profiles. Corresponding Zn^{2+} diffusion coefficient in discharging (e) and charging (f) processes.

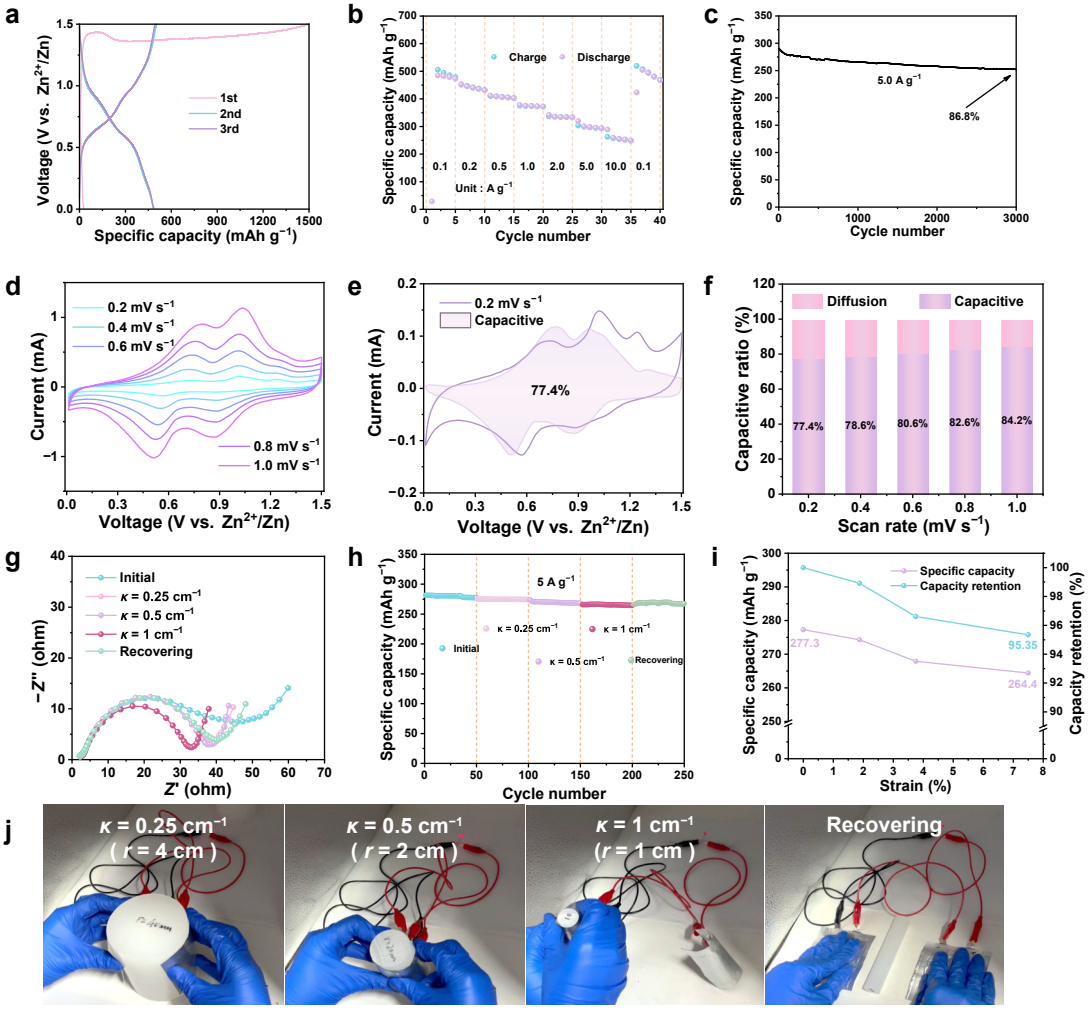

Figure 6 Characterizations of pouch cells employing VN/CF-600 cathode. (a) GCD curves at 0.1 A g^{-1}. (b) Rate capability. (c) Cycle performance at 5 A g^{-1}. (d) CV curves at different scan rates from 0.2 to 1.0 mV s^{-1}. (e) Capacitive contributions at 0.2 mV s^{-1}. (f) Capacity contribution ratios at various scan rates. Nyquist plots (g) and cycling performance (h) in different bending states. (i) Specific capacity under different strains. (j) Experiment demonstrating light-emitting diode lit by two integrated pouch cells in bending deformation at different degrees of curvature.

in the pouch cell configuration. This finding is consistent with the data from the coin cell. The pouch cell delivers specific discharge capacities of 472.9, 431.4, 402.7, 371.8, 333.1, 293.8, and 249.7 mAh g^{-1} at 0.1, 0.2, 0.5, 1, 2, 5, and 10 A g^{-1}, respectively (Fig. 6b). The corresponding capacity is approximately 12.8 mAh at 0.1 A g^{-1}. Notably, the VN/CF-600 electrode in the pouch cell has a mass of 27.19 mg, which is significantly higher than that in the coin cells, yet it maintains excellent rate performance comparable to that of the coin cell. This sustained performance under high mass-loading is attributed to the VN structure with abundant oxygen defects and vertically aligned nanosheet arrays, which facilitate fast ion diffusion, highlighting the potential of VN/CF-600 for practical applications. The pouch cell also demonstrates excellent cycling stability, with a capacity retention of 86.8% after 3000 cycles at 5 A g^{-1}. This performance highlights the good stability of the free-standing VN/CF-600 cathode for device applications. The pouch cell exhibits shape-invariant CV curves across all scan rates (Fig. 6d), indicating stable electrochemical processes. It has a capacitance contribution of 77.4% at 0.2 mV s^{-1} and 84.2% at 1.0 mV s^{-1}, revealing the capacitive-dominated storage. To evaluate the performance under bending deformation, the pouch cells were wound around cylinders with radii of 4, 2, and 1 cm during testing, corresponding to a curvature (κ) of 0.25, 0.50, and 1.00 cm^{-1}, respectively. The EIS results show that the charge-transfer and ion-diffusion impedances decrease gradually with an increase in the curvature from 0.25 to 1 cm^{-1} (Fig. 6g). This impedance reduction is attributed to enhanced electrode–separator contact, which shortens the charge-/ion-transport pathways. Fifty repeated bending tests were also conducted at curvatures of 0.25, 0.5, and 1 cm^{-1}. After these tests, the recorded specific capacities were 274.3, 267.8, and 264.4 mAh g^{-1}, corresponding to capacity retention rates of 98.99%, 96.6%, and 95.3%, respectively (Fig. 6h), demonstrating exceptional mechanical stability. Quantitative strain analysis using the formula $\varepsilon = t\kappa/2$ (where t is the thickness[91–92]) reveals an ultrahigh capacity retention of 98.92%, 96.61%, and 95.35% at applied strains of 1.88%, 3.75%, and 7.5%, respectively (Fig. 6i). The pouch cell

stably powers a light-emitting diode (LED) across deformation gradients (Fig. 6j). These results collectively demonstrate the exceptional mechanical and electrochemical stability of free-standing VN/CF-600, confirming its promise for flexible aqueous zinc-ion batteries.

4 Conclusion

In summary, a free-standing VN/carbon fiber with oxygen defects and a vertically aligned, porous nanosheet architecture was constructed via V_2O_5 templating and NH_3 treatment. Abundant oxygen defects were generated in VN by the removal of water-of-crystallization and V_2O_5-to-VN phase transformation during high-temperature annealing under NH_3 atmosphere. The optimized structure effectively enhances the kinetics of ion transport, leading to superior rate capability in AZIBs. Moreover, the corresponding pouch cells exhibit excellent and stable performance even under various bending deformations. This study provides a systematic framework for constructing advanced flexible AZIBs.

Acknowledgements

None.

Author contribution statement

Zhouyang Qin: conceptualization, methodology, data curation, formal analysis, writing original draft. **Gaoxu Han**: investigation. **Yilin Yang**: investigation. **Wenjie Zhang**: methodology, investigation, writing-review & editing. **Ruitao Lv**: resources, supervision. **Wanci Shen**: resources, methodology. **Zheng-Hong Huang**: project administration, conceptualization, methodology, resources, writing-review & editing. All the authors have approved the final manuscript.

Data availability

The data that supports the findings of this study is available from the corresponding author upon reasonable request.

Declaration of competing interest

All the contributing authors report no conflicts of interest in this work.

Funding

This work is granted by the National Natural Science Foundation of China (NSFC; Grant No. 52172047) and NSFC Original Exploration Program (Grant No. 52450072).

Use of AI statement

None.

Electronic Supplementary Material: Supplementary material is available in the online version of this article at https://doi.org/10.26599/EMD.2026.9370086

References

[1] He, J. Y., Cao, L. Q., Cui, J. J., Fu, G. W., Jiang, R. Y., Xu, X., Guan, C. (2024). Flexible energy storage devices to power the future. *Adv. Mater.* 36, 2306090.

[2] Zhang, W. J., Shen, W. C., Weng, Y. Q., Lv, R. T., Kang, F. Y., Huang, Z. H. (2019). Steam selective etching: a strategy to effectively enhance the flexibility and suppress the volume change of carbonized paper-supported electrodes. *ACS Nano* 13, 5731–5741.

[3] Xiao, B. H., Xiao, K., Li, J. X., Xiao, C. F., Cao, S. S., Liu, Z. Q. (2024). Flexible electrochemical energy storage devices and related applications: recent progress and challenges. *Chem. Sci.* 15, 11229–11266.

[4] Li, H. F., Tang, Z. J., Liu, Z. X., Zhi, C. Y. (2019). Evaluating flexibility and wearability of flexible energy storage devices. *Joule* 3, 613–619.

[5] Panigrahi, K., Howli, P., Chattopadhyay, K. K. (2020). 3D network of V_2O_5 for flexible symmetric supercapacitor. *Electrochim. Acta* 337, 135701.

[6] Kumar, Y. A., Sambasivam, S., Hira, S. A., Zeb, K., Uddin, W., Krishna, T. N. V., Kumar, K. D., Obaidat, I. M., Kim, H. J. (2020). Boosting the energy density of highly efficient flexible hybrid supercapacitors via selective integration of hierarchical nanostructured energy materials. *Electrochim. Acta* 364, 137318.

[7] Paul, R., Roy, A. K. (2021). BN-codoped CNT based nanoporous brushes for all-solid-state flexible supercapacitors at elevated temperatures. *Electrochim. Acta* 365, 137345.

[8] Liu, T., Chen, X., Tervoort, E., Kraus, T., Niederberger, M. (2021). Design and fabrication of transparent and stretchable zinc ion batteries. *ACS Appl. Energy Mater.* 4, 6166–6179.

[9] Tamilselvan, M., Sreekanth, T. V. M., Yoo, K., Kim, J. (2020). Binder-free coaxially grown V_6O_{13} nanobelts on carbon cloth as cathodes for highly reversible aqueous zinc ion batteries. *Appl. Surf. Sci.* 529, 147077.

[10] Zhang, G. J., Yin, K. B., Zheng, A. Q., Pan, R., Cui, F. H., Jiang, Z. J., Huang, Y. H., Tan, Z. Y., Sun, L. T. (2023). 1D/2D heterostructure induced built-in electric field accelerate the reaction kinetics of MnO_2/MXene paper-like film for advanced flexible zinc-ion batteries. *Electrochim. Acta* 469, 143261.

[11] Tang, F. J., Zhou, W. J., Chen, M. F., Chen, J. Z., Xu, J. L. (2019). Flexible free-standing paper electrodes based on reduced graphene oxide/δ-$Na_xV_2O_5{\cdot}nH_2O$ nanocomposite for high-performance aqueous zinc-ion batteries. *Electrochim. Acta* 328, 135137.

[12] Hieu, L. T., So, S., Kim, I. T., Hur, J. (2021). Zn anode with flexible β-PVDF coating for aqueous Zn-ion batteries with long cycle life. *Chem. Eng. J.* 411, 128584.

[13] Kim, C., Ahn, B. Y., Wei, T. S., Jo, Y., Jeong, S., Choi, Y., Kim, I. D., Lewis, J. A. (2018). High-power aqueous zinc-ion batteries for customized electronic devices. *ACS Nano* 12, 11838–11846.

[14] Lee, Y. G., Lee, J., An, G. H. (2021). Free-standing manganese oxide on flexible graphene films as advanced electrodes for stable, high energy-density solid‐state zinc-ion batteries. *Chem. Eng. J.* 414, 128916.

[15] Huang, J. T., Zhong, Y. P., AlMasoud, N., Alomar, T. S., Xie, Y. M., Lu, B. G., Liang, S. Q., El-Bahy, Z. M., Tian, S. Y., Zhou, J. (2025). Tailored fluoroborate-based electrolyte with fast interphase formation kinetics toward stable Ah-level zinc batteries. *Adv. Powder Mater.* 4, 100306.

[16] Hu, X. T., Lai, G. J., Liu, Y. Y., Zhou, P., Lu, B. G., El-Bahy, Z. M., Ebaid, M. S., Chen, L. N., Zhou, J. (2025). Design of dual-electrode interfacial kinetics regulator for long-lasting Ah-level zinc-iodine batteries. *eScience* 5, 100455.

[17] Zhang, H., Liu, X., Li, H. H., Hasa, I., Passerini, S. (2021). Challenges and strategies for high‐energy aqueous electrolyte rechargeable batteries. *Angew. Chem. Int. Ed.* 60, 598–616.

[18] Zhang, K. Q., Wang, L. Y., Ma, C. L., Yuan, Z. J., Wu, C., Ye, J. L., Wu, Y. P. (2024). A comprehensive evaluation of battery tech-

清華大學出版社 Tsinghua University Press | SciOpen

nologies for high-energy aqueous batteries. *Small* 20, 2309154.
[19] Zhang, F. L., Zhang, W. C., Wexler, D., Guo, Z. P. (2022). Recent progress and future advances on aqueous monovalent-ion batteries towards safe and high-power energy storage. *Adv. Mater.* 34, 2107965.
[20] Wang, X., Liu, L. Y., Hu, Z. W., Peng, C. C., Han, C., Li, W. J. (2023). High energy density aqueous zinc-chalcogen (S, Se, Te) batteries: recent progress, challenges, and perspective. *Adv. Energy Mater.* 13, 2302927.
[21] Zhang, Y. L., Ye, R. J., Henkensmeier, D., Hempelmann, R., Chen, R. Y. (2018). "Water-in-ionic liquid" solutions towards wide electrochemical stability windows for aqueous rechargeable batteries. *Electrochim. Acta* 263, 47–52.
[22] Alfaruqi, M. H., Islam, S., Putro, D. Y., Mathew, V., Kim, S., Jo, J., Kim, S., Sun, Y. K., Kim, K., Kim, J. (2018). Structural transformation and electrochemical study of layered MnO_2 in rechargeable aqueous zinc-ion battery. *Electrochim. Acta* 276, 1–11.
[23] Poyraz, A. S., Laughlin, J., Zec, Z. (2019). Improving the cycle life of cryptomelane type manganese dioxides in aqueous rechargeable zinc ion batteries: the effect of electrolyte concentration. *Electrochim. Acta* 305, 423–432.
[24] Shen, Q., Zhao, Y. H., Yuan, Y., Chen, G., Tan, L. C., Wu, X. L., Guo, L., Guo, Z. H., Chen, C. X. (2025). Enhancing zinc ion hybrid supercapacitors *via* structural expansion and N, S co-doping of porous carbon. *J. Power Sources* 659, 238440.
[25] Zhao, H. C., Bai, Y., Li, Y., Zhao, W. B., Ren, H. X., Wang, X. R., Wu, C. (2022). Insight into thermal analysis kinetics of surface protected $LiNi_{0.8}Co_{0.15}Al_{0.05}O_2$ cathode for safe lithium-ion batteries. *Energy Storage Mater.* 49, 409–420.
[26] Li, Y., Wang, Z. H., Cai, Y., Pam, M. E., Yang, Y. K., Zhang, D. H., Wang, Y., Huang, S. Z. (2022). Designing advanced aqueous zinc-ion batteries: principles, strategies, and perspectives. *Energy Environ. Mater.* 5, 823–851.
[27] Dai, C. L., Hu, L. Y., Jin, X. T., Zhao, Y., Qu, L. T. (2021). The emerging of aqueous zinc‐based dual electrolytic batteries. *Small* 17, 2008043.
[28] Hashemi, A. B., Kasiri, G., La Mantia, F. (2017). The effect of polyethyleneimine as an electrolyte additive on zinc electrodeposition mechanism in aqueous zinc-ion batteries. *Electrochim. Acta* 258, 703–708.
[29] Lee, Y. H., Jeoun, Y., Kim, J. H., Shim, J., Ahn, K. S., Yu, S. H., Sung, Y. E. (2024). Selective ion transport layer for stable aqueous zinc-ion batteries. *Adv. Funct. Mater.* 34, 2310884.
[30] Xue, P., Guo, C., Tan, L. C. (2023). Hydrogen-bonding crosslinking MXene to highly mechanically stable and super-zincophilic host for stable Zn metal anode. *Chem. Eng. J.* 472, 145056.
[31] Lv, T. T., Peng, Y., Zhang, G. X., Jiang, S., Yang, Z. L., Yang, S. Y., Pang, H. (2023). How about vanadium-based compounds as cathode materials for aqueous zinc ion batteries?. *Adv. Sci.* 10, 2206907.
[32] Tang, F., Gao, J. Y., Ruan, Q. Y., Wu, X. W., Wu, X. S., Zhang, T., Liu, Z. X., Xiang, Y. H., He, Z. Q., Wu, X. M. (2020). Graphene-wrapped MnO/C composites by MOFs-derived as cathode material for aqueous zinc ion batteries. *Electrochim. Acta* 353, 136570.
[33] Menart, S., Pirnat, K., Pahovnik, D., Dominko, R. (2023). Triquinoxalinediol as organic cathode material for rechargeable aqueous zinc-ion batteries. *J. Mater. Chem. A* 11, 10874–10882.
[34] Cheng, Z. X., Qi, W. L., Pang, C. H., Thomas, T., Wu, T., Liu, S. Q., Yang, M. H. (2021). Recent advances in transition metal nitride-based materials for photocatalytic applications. *Adv. Funct. Mater.* 31, 2100553.
[35] Eklund, P., Kerdsongpanya, S., Alling, B. (2016). Transition-metal-nitride-based thin films as novel energy harvesting materials. *J. Mater. Chem. C* 4, 3905–3914.
[36] Eck, B., Dronskowski, R., Takahashi, M., Kikkawa, S. (1999). Theoretical calculations on the structures, electronic and magnetic properties of binary 3d transition metal nitrides. *J. Mater. Chem.* 9, 1527–1537.
[37] Häglund, J., Grimvall, G., Jarlborg, T., Guillermet, A. F. (1991). Band structure and cohesive properties of 3*d*-transition-metal carbides and nitrides with the NaCl-type structure. *Phys. Rev. B* 43, 14400–14408.
[38] Liu, Y. X., Zhang, J., Liu, Y., Zhang, M. C., Pan, Z. H., Cai, K. F. (2024). Controllable design of metal-organic framework-derived vanadium oxynitride for high-capacity and long-cycle aqueous Zn-ion batteries. *Small* 20, 2401922.
[39] Zhao, Z. W., Qian, Y. J., Zhao, X. M., Yang, B. Z., Wang, S., Lu, X. P., Guan, C. L. (2020). Reaction kinetics and properties of VN/CrN nanocomposite via microwave in situ synthesis. *Int. J. Refract. Met. Hard Mater.* 92, 105326.
[40] Zeng, F. Y., Lu, T., He, W. X., Chu, S. L., Qu, Y. H., Pan, Y. (2021). *In-situ* carbon encapsulation of ultrafine VN in yolk-shell nanospheres for highly reversible sodium storage. *Carbon* 175, 289–298.
[41] Guo, C., Yi, S. J., Si, R., Xi, B. J., An, X. G., Liu, J., Li, J. F., Xiong, S. L. (2022). Advances on defect engineering of vanadium-based compounds for high-energy aqueous zinc-ion batteries. *Adv. Energy Mater.* 12, 2202039.
[42] Bai, Y. C., Luo, L., Song, W. L., Man, S. S., Zhang, H., Li, C. M. (2024). Nitrogen-vacancy-rich VN clusters embedded in carbon matrix for high-performance zinc ion batteries. *Adv. Sci.* 11, 2308668.
[43] Tang, B., Xiang, Y. S., Li, X. L., Xu, C. H., Wang, R. H. (2025). VN_xO_y@C nanowires: a high-performance cathode material for aqueous zinc-ion batteries with dual-redox reaction mechanisms. *J. Mater. Chem. A* 13, 30019–30028.
[44] Ding, J. W., Du, Z. G., Li, B., Wang, L. Z., Wang, S. W., Gong, Y. J., Yang, S. B. (2019). Unlocking the potential of disordered rock-salts for aqueous zinc-ion batteries. *Adv. Mater.* 31, 1904369.
[45] Xie, X. F., Fang, G. Z., Xu, W. J., Li, J. L., Long, M. Q., Liang, S. Q., Cao, G. Z., Pan, A. Q. (2021). In situ defect induction in close-packed lattice plane for the efficient zinc ion storage. *Small* 17, 2101944.
[46] Zheng, W., Sun, Z. H., Gu, Z. Y., Wu, X. L., Niu, L. (2025). Recent advances in vanadium-based cathode materials for aqueous zinc-ion batteries: from fundamentals to practical applications. *Adv. Mater. Technol.* 10, 2500320. doi: 10.1002/admt.202500320.
[47] Jia, X. X., Liu, C. F., Neale, Z. G., Yang, J. H., Cao, G. Z. (2020). Active materials for aqueous zinc ion batteries: synthesis, crystal structure, morphology, and electrochemistry. *Chem. Rev.* 120, 7795–7866.
[48] Du, M., Miao, Z. Y., Li, H. Z., Sang, Y. H., Liu, H., Wang, S. H. (2021). Strategies of structural and defect engineering for high-performance rechargeable aqueous zinc-ion batteries. *J. Mater. Chem. A* 9, 19245–19281.
[49] Yuan, Z. Y., Yang, X. H., Lin, C. Y., Xiong, P. X., Su, A. M., Fang, Y. X., Chen, X. C., Fan, H. S., Xiao, F. Y., Wei, M. D., et al. (2023). Progressive activation of porous vanadium nitride microspheres with intercalation-conversion reactions toward high performance over a wide temperature range for zinc-ion batteries. *J. Colloid Interface Sci.* 640, 487–497.
[50] Fan, L., Ru, Y., Xue, H. G., Pang, H., Xu, Q. (2020). Vanadium-based materials as positive electrode for aqueous zinc-ion batteries. *Adv. Sustain. Syst.* 4, 2000178.
[51] Yang, S. N., Zhao, S. S., Chen, S. M. (2023). Recent advances in electrospinning nanofiber materials for aqueous zinc ion batteries. *Chem. Sci.* 14, 13346–13366.
[52] Wang, X., Zhang, Z. C. Y., Xi, B. J., Chen, W. H., Jia, Y. X., Feng, J. K., Xiong, S. L. (2021). Advances and perspectives of cathode storage chemistry in aqueous zinc-ion batteries. *ACS Nano* 15, 9244–9272.
[53] Ding, J. W., Gao, H. G., Ji, D. F., Zhao, K., Wang, S. W., Cheng, F. Y. (2021). Vanadium-based cathodes for aqueous zinc-ion batteries: from crystal structures, diffusion channels to storage mecha-

nisms. *J. Mater. Chem. A* 9, 5258–5275.
[54] Chang, J. Q., Fu, X. P., Liu, J. H., Li, C. X., Feng, G. D., Bao, F. X., Guo, W. (2025). Vanadium nitride oxide quantum dots modified nitrogen-doped graphene as cathode for high-performance aqueous zinc-ion batteries. *J. Power Sources* 639, 236649.
[55] Bian, Y. J., Hu, R. T., Wang, H. Y., Gong, J. X., Liu, W. F., Fu, M. Q., Wang, W. W., Yan, J. (2025). Developing an in situ polyoxovanadate to vanadium nitride/carbon conversion strategies in manufacture aqueous zinc ion batteries cathode with ultrahigh rate capability. *Adv. Funct. Mater.* 35, 2418671.
[56] Luo, S. J., Cui, J. Y., Liang, S. J., Guo, Y., Yuan, B. H., Xu, L., Zheng, R., Li, J. M., Yang, W. P., Chen, M. L., et al. (2024). Carbon-enveloped pea-shaped vanadium nitride nanorods for aqueous zinc ion batteries. *J. Mater. Chem. C* 12, 6153–6160.
[57] Yao, X. C., Khanam, Z., Li, C. L., Koroma, M., Ouyang, T., Hu, Y. W., Shen, K., Balogun, M. S. (2024). Unlatching the additional zinc storage ability of vanadium nitride nanocrystallites. *Small* 20, 2312036.
[58] Chi, J. X., Xu, H., Wang, J. Q., Tang, X. Q., Yang, S., Ding, B., Dou, H., Zhang, X. G. (2023). *In situ* electrochemically oxidative activation inducing ultrahigh rate capability of vanadium oxynitride/carbon cathode for zinc-ion batteries. *ACS Appl. Mater. Interfaces* 15, 4061–4070.
[59] Fang, G. Z., Liang, S. Q., Chen, Z. X., Cui, P. X., Zheng, X. S., Pan, A. Q., Lu, B. G., Lu, X. H., Zhou, J. (2019). Simultaneous cationic and anionic redox reactions mechanism enabling high-rate long-life aqueous zinc-ion battery. *Adv. Funct. Mater.* 29, 1905267.
[60] Chen, D., Lu, M. J., Wang, B. R., Chai, R. Q., Li, L., Cai, D., Yang, H., Liu, B. K., Zhang, Y. P., Han, W. (2021). Uncover the mystery of high-performance aqueous zinc-ion batteries constructed by oxygen-doped vanadium nitride cathode: cationic conversion reaction works. *Energy Storage Mater.* 35, 679–686.
[61] Wang, H. P., Miao, W. X., Liu, Z. Y., Tao, B., Sun, K. J., Peng, H., Ma, G. F. (2025). Design of oxygen vacancies homologous heterojunction promoted reversible zinc ion storage. *Rare Met.* 44, 7220–7229.
[62] Chen, J. J., Guo, K. Y., Ren, T. Z., Feng, G. D., Guo, W., Bao, F. X. (2025). Aluminium-doped vanadium nitride as cathode material for high-performance aqueous zinc-ion batteries. *J. Power Sources* 626, 235751.
[63] Wang, H. P., Hou, W. B., Wang, X., Xie, X., Peng, H., Ma, G. F., Zhu, L., Xu, Y. X. (2025). Construction of MOF-derived vanadium nitride decorated micro/mesoporous carbon nanofibers for aqueous zinc-ion batteries. *Chem. -Eur. J.* 31, e202403903.
[64] Zhang, Y. M., Jiang, S. Y., Li, Y. L., Ren, X. Z., Zhang, P. X., Sun, L. N., Yang, H. Y. (2023). In situ grown hierarchical electrospun nanofiber skeletons with embedded vanadium nitride nanograins for ultra-fast and super-long cycle life aqueous Zn-ion batteries. *Adv. Energy Mater.* 13, 2202826.
[65] Su, Q. S., Rong, Y., Chen, H. Z., Wu, J., Yang, Z. H., Deng, L., Fu, Z. M. (2021). Carbon-doped vanadium nitride used as a cathode of high-performance aqueous zinc ion batteries. *Ind. Eng. Chem. Res.* 60, 12155–12165.
[66] Wu, J., Yu, X., Liang, H. H., Long, Y. N., Yang, Z. H. (2023). Ultrathin nanosheet assemblies of three-dimensional spongy carbon/nitrogen-doped vanadium nitride cathode for high-performance aqueous zinc-ion batteries. *Ind. Eng. Chem. Res.* 62, 10861–10871.
[67] Liu, X. Q., Li, G. S., Zhang, X., Wu, J. J., Yu, C., Peng, L. F., Zhang, D., Li, L. P. (2024). Unlocking a new storage mechanism of high performance VN@N/S-C cathode: role of electrochemical reduction. *J. Power Sources* 590, 233796.
[68] Wang, D. P., Wen, C., Xu, M. T., Wen, W. H., Tu, J., Zhu, G. Y., Zhou, Z. J., Tu, Z. K., Fu, Y. Q. (2025). In-situ construction of VN-based heterostructure with high interfacial stability and porous channel effect for efficient zinc ion storage. *J. Mater. Sci. Technol.* 224, 205–215.
[69] Niu, Y., Xu, W. Q., Ma, Y. J., Gao, Y., Li, X. L., Li, L. D., Zhi, L. J. (2022). Layer-by-layer stacked vanadium nitride nanocrystals/N-doped carbon hybrid nanosheets toward high-performance aqueous zinc-ion batteries. *Nanoscale* 14, 7607–7612.
[70] Park, J. S., Wang, S. E., Jung, D. S., Lee, J. K., Kang, Y. C. (2022). Nanoconfined vanadium nitride in 3D porous reduced graphene oxide microspheres as high-capacity cathode for aqueous zinc-ion batteries. *Chem. Eng. J.* 446, 137266.
[71] Ma, H., Tang, C. Y., Zhang, F. W., Tao, Z. Q., Liu, J. H., Yan, B., Tao, H. C. (2025). High-Mass-Loading vanadium nitride /N-doped rGO cathode for fast and stable Zinc-Ion storage. *Appl. Surf. Sci.* 710, 163917.
[72] Chen, H. Z., Yang, Z. H., Wu, J., Rong, Y., Deng, L. (2021). Industrial VN@reduced graphene oxide cathode for aqueous zinc ion batteries with high rate capability and long cycle stability. *J. Power Sources* 507, 230286.
[73] Chen, H. Z., Yang, Z. H., Wu, J. (2022). Vanadium nitride@nitrogen-doped graphene as zinc ion battery cathode with high rate capability and long cycle stability. *Ind. Eng. Chem. Res.* 61, 2955–2962.
[74] Cao, Y. Y., Wei, S. Q., Xia, Y. J., Zhou, Q., Wang, Y. X., Xu, W. J., Wang, C. D., Chen, S. M., Song, L. (2024). Nitridation-boosted V e_g occupation of a VN@CNT flexible electrode for high-rate Zn-ion hybrid supercapacitors. *J. Mater. Chem. A* 12, 32895–32903.
[75] Du, W. Y., Miao, L., Song, Z. Y., Zheng, X. W., Lv, Y. K., Zhu, D. Z., Gan, L. H., Liu, M. X. (2022). Kinetics-driven design of 3D VN/MXene composite structure for superior zinc storage and charge transfer. *J. Power Sources* 536, 231512.
[76] Zhao, R., Liu, C., Zhu, Y. R., Zou, G. Q., Hou, H. S., Ji, X. B. (2024). Pathways for MXenes in solving the issues of zinc-ion batteries: achievements and perspectives. *Adv. Funct. Mater.* 34, 2316643.
[77] Liu, Y. Z., Lin, L., Zhang, T. S., Xue, Z. Q., Liu, J., Chao, D. L., Sun, X. Q. (2024). A cyano cobalt "electron transfer bridge" boosting the two-electron reaction of a MnO_2 cathode with long lifespan in aqueous zinc batteries. *Energy Environ. Sci.* 17, 2521–2529.
[78] Yang, H. L., Ning, P. G., Wen, J. W., Xie, Y. B., Su, C. L., Li, Y. P., Cao, H. B. (2021). Structure control in VN_xO_y by hydrogen bond association extraction for enhanced zinc ion storage. *Electrochim. Acta* 389, 138722.
[79] Qin, H. Q., Mo, Z. Z., Lu, J., Sui, X., Song, Z. F., Chen, B., Zhang, Y. J., Zhang, Z. J., Lei, X. X., Lu, A. J., et al. (2024). Ultrafast transformation of natural graphite into self-supporting graphene as superior anode materials for lithium-ion batteries. *Carbon* 216, 118559.
[80] Xu, Y., Fan, G. L., Sun, P. X., Guo, Y., Wang, Y. Y., Gu, X. J., Wu, L. M., Yu, L. (2023). Carbon nitride pillared vanadate via chemical pre-intercalation towards high-performance aqueous zinc-ion batteries. *Angew. Chem. Int. Ed.* 62, e202303529.
[81] Lu, H. B., Zhang, Z. C. Y., An, X. G., Feng, J. K., Xiong, S. L., Xi, B. J. (2023). In situ electrochemically transforming VN/V_2O_3 heterostructure to highly reversible V_2NO for excellent zinc ion storage. *Small Struct.* 4, 2300191.
[82] Li, Y., Yang, W., Yang, W., Huang, Y. F., Wang, G. X., Xu, C. J., Kang, F. Y., Dong, L. B. (2021). High-performance zinc-ion batteries enabled by electrochemically induced transformation of vanadium oxide cathodes. *J. Energy Chem.* 60, 233–240.
[83] Liu, S. D., Kang, L., Kim, J. M., Chun, Y. T., Zhang, J., Jun, S. C. (2020). Recent advances in vanadium-based aqueous rechargeable zinc-ion batteries. *Adv. Energy Mater.* 10, 2000477.
[84] Zhang, Z. Y., Lee, C. S., Zhang, W. J. (2017). Vertically aligned graphene nanosheet arrays: synthesis, properties and applications in electrochemical energy conversion and storage. *Adv. Energy Mater.* 7, 1700678.
[85] Zhu, J. X., Sakaushi, K., Clavel, G., Shalom, M., Antonietti, M., Fellinger, T. P. (2015). A general salt-templating method to fabricate vertically aligned graphitic carbon nanosheets and their metal carbide hybrids for superior lithium ion batteries and water splitting. *J. Am. Chem. Soc.* 137, 5480–5485.
[86] Zhu, S., Sheng, J., Ni, J. F., Li, Y. (2021). 3D vertical arrays of

清華大學出版社 Tsinghua University Press | SciOpen

nanomaterials for microscaled energy storage devices. *Acc. Mater. Res.* 2, 1215–1226.

[87] Zhu, Y., Ju, Z. Y., Zhang, X., Lutz, D. M., Housel, L. M., Zhou, Y. G., Takeuchi, K. J., Takeuchi, E. S., Marschilok, A. C., Yu, G. H. (2020). Evaporation-induced vertical alignment enabling directional ion transport in a 2D-nanosheet-based battery electrode. *Adv. Mater.* 32, 1907941.

[88] Dai, H. H., Zhao, X., Xu, H., Yang, J., Zhou, J. Y., Chen, Q., Sun, G. Z. (2022). Design of vertically aligned two-dimensional heterostructures of rigid Ti_3C_2TX MXene and pliable vanadium pentoxide for efficient lithium ion storage. *ACS Nano* 16, 5556–5565.

[89] Ebner, M., Chung, D. W., García, R. E., Wood, V. (2014). Tortuosity anisotropy in lithium-ion battery electrodes. *Adv. Energy Mater.* 4, 1301278.

[90] Chen, Y. W., Ma, D. T., Shen, S. C., Deng, P. H., Zhao, Z. H., Yang, M., Wang, Y. Y., Mi, H. W., Zhang, P. X. (2023). New insights into high-rate and super-stable aqueous zinc-ion batteries via the design concept of voltage and solvation environment coordinated control. *Energy Storage Mater.* 56, 600–610.

[91] Park, S. I., Ahn, J. H., Feng, X., Wang, S. D., Huang, Y. G., Rogers, J. A. (2008). Theoretical and experimental studies of bending of inorganic electronic materials on plastic substrates. *Adv. Funct. Mater.* 18, 2673–2684.

[92] Paeng, D., Yoo, J. H., Yeo, J., Lee, D., Kim, E., Ko, S. H., Grigoropoulos, C. P. (2015). Low-cost facile fabrication of flexible transparent copper electrodes by nanosecond laser ablation. *Adv. Mater.* 27, 2762–2767.

Open Access This article is licensed under a Creative Commons Attribution 4.0 International License (CC BY 4.0), which permits reusers to distribute, remix, adapt, and build upon the material in any medium or format, so long as attribution is given to the original author(s) and the source, a link to the license is provided, and any changes made are indicated. See https://creativecommons.org/licenses/by/4.0/

© The author(s) 2026. Published by Tsinghua University Press.